



Article

The Study on Anomalies of the Geomagnetic Topology Network Associated with the 2022 Ms6.8 Luding Earthquake

Zining Yu ¹, Xilong Jing ¹, Xianwei Wang ¹, Chengquan Chi ² and Haiyong Zheng ^{1,*}

¹ College of Electronic Engineering, Ocean University of China, Qingdao 266404, China; yuzining@ouc.edu.cn (Z.Y.); jingxilong@stu.ouc.edu.cn (X.J.); wangxianwei@stu.ouc.edu.cn (X.W.)

² School of Information Science and Technology, Hainan Normal University, Haikou 571158, China; chicqhainnu@gmail.com

* Correspondence: zhenghaiyong@ouc.edu.cn

Abstract: On 5 September 2022, the Ms 6.8 Luding earthquake occurred at 29.59°N and 102.08°E in China. To investigate the variations in geomagnetic signals before the earthquake, this study analyzes the geomagnetic data from nine stations around the epicenter. First, we apply the Multi-channel Singular Spectrum Analysis to reconstruct the periodic components of the geomagnetic data from multiple stations. Second, we employ K-means clustering to rule out the possibility of occasional anomalies caused by a single station. Subsequently, we construct a geomagnetic topology network considering the remaining stations. Network centrality is defined as a measure of overall network connectivity, where the higher the correlation between multiple stations, the greater the network centrality. Finally, we examine the network centrality 45 days before and 15 days after the Luding earthquake. The results show that several anomalies in network centrality are extracted about one week before the earthquake. We further validate the significance of the anomalies in terms of time as well as space and verify the utility of the centrality anomalies through the SEA technique. The anomalies are found to have a statistical correlation with the earthquake event. We consider that this study provides a new way and a novel observational perspective for earthquake precursor analysis of ground-based magnetic data.

Keywords: geomagnetic signals; Luding earthquake; multiple stations; topology network



Citation: Yu, Z.; Jing, X.; Wang, X.; Chi, C.; Zheng, H. The Study on Anomalies of the Geomagnetic Topology Network Associated with the 2022 Ms6.8 Luding Earthquake. *Remote Sens.* **2024**, *16*, 1613. <https://doi.org/10.3390/rs16091613>

Academic Editors: Dedalo Marchetti and Mehdi Akhoondzadeh

Received: 29 February 2024

Revised: 15 April 2024

Accepted: 24 April 2024

Published: 30 April 2024



Copyright: © 2024 by the authors. Licensee MDPI, Basel, Switzerland. This article is an open access article distributed under the terms and conditions of the Creative Commons Attribution (CC BY) license (<https://creativecommons.org/licenses/by/4.0/>).

1. Introduction

Monitoring earthquakes plays a crucial role in the early detection and warning of earthquake activities. With the development of monitoring technologies, seismo-electromagnetic (EM) phenomena have gradually come to be considered the most promising candidates for short-term earthquake prediction [1–4]. In particular, the development of the lithosphere–atmosphere–ionosphere coupling (LAIC) mechanism has brought us new findings and understandings of the process of earthquake preparation [5–7]. Currently, the most reliable methods of recognizing earthquake precursors are considered to be the multi-component and multi-method analysis [8–11]. For example, Pulinetz et al. [12] adopted a multi-method way to validate the precursory phenomena in the ionospheric of the 1999 Hector Mine and 2019 Ridgecrest earthquakes: firstly, they computed the time-series of $\Delta TEC\%$ around the earthquakes and found there are likely positive night-time deviations before the earthquakes; secondly, they started cognitive recognition through the precursor mask approach [13], which is a special visualization pattern analysis to check the possible precursors; thirdly, they revealed the increased spatial variability by calculating the root mean square deviation (RMSD) to further validate the precursor mask; next, to further prove that suspicious variations, they used a cross-correlation technique to reveal the reliability of the precursor mask [14]; and lastly, they demonstrated the precursors based on the physical mechanisms of their generation and the morphology of their behavior during the precursory period. What is more, there is also a multi-component way; Liu

et al. [15] provided an analysis of the seismic Precursor Identification (CAPRI) algorithm to detect anomalous changes associated with the Ms 8.0 2008 Wenchuan and Ms 7.0 2013 Lushan earthquakes based on four datasets in the atmosphere. Finally, they found a chain of processes that occurred within two months before the earthquakes and concluded that the extracted anomalies may be related to the same process.

EM phenomena closest to lithospheric earthquakes, usually concerning the ground-based magnetic field, have also followed this multi-component and multi-method approach to study the precursor anomaly [16–19]. Currently, some researchers are focused primarily on a united study on the results of independent stations. Hattori et al. [4] selected six stations in the Izu and Boso Peninsulas and applied wavelet transformations at each station to evaluate anomalies in the 0.01 Hz band of ULF geomagnetic data individually, to illustrate that the unusual enhancements in geomagnetic energy preceding the main earthquake events may be a precursor. Then, Guo et al. [20] utilized an enhanced principal component analysis method for each station's geomagnetic data to extract anomalous signals from 20 high-quality AETA stations, and confirmed a relationship between EM anomalies and local earthquake events. However, earthquake preparation is a systematic self-organizing process [21], which may have been recorded at the observational data level. Thus, some researchers analyzed the correlation of EM data across multiple stations. Wen et al. [22] calculated the cross-correlation between eleven stations of the geomagnetic data from the two frequency bands to determine whether the correlation is associated with seismo-magnetic anomalies, and they found that decreased values of the cross-correlation and earthquake occurrences yield a good agreement in the time scale. Pulinets et al. [14] also used cross-correlation as an effective skill for determining precursors. However, the cross-correlation between stations is calculated in pairs, and information on the cross-correlation coefficients is very limited when discussing dense stations.

Therefore, we adopt a multi-station analysis approach at the data level through Multi-channel Singular Spectrum Analysis (MSSA) [23]. MSSA is particularly suitable for the multi-scale decomposition of spatiotemporal data and managing multivariate time series by estimating periodic components and trends and reducing noise [24,25]. Subsequently, to address the limitations of cross-correlation, we construct a topology network to analyze the correlation of spatiotemporal features in multi-station data. Topology networks have many properties that can clarify diverse correlation information based on graph theory, such as centrality degree, density, and small world [26–29], regardless of the number of stations.

In this paper, we investigate the geomagnetic observations related to the Luding Ms 6.8 earthquake from the Acoustic and Electromagnetics to Artificial Intelligence (AETA) system. AETA is a multi-component earthquake-monitoring system, which has been installed in over 200 sites nationwide in China [30]. To date, there have been many advances in the study of earthquake precursors based on the AETA system [31,32]. This work is organized as follows. Sections 2 and 3 describe the observations and analysis methods. Section 4 shows our results and analysis. In Section 5, we provide a discussion on whether the extracted network anomalies are associated with the Luding earthquake. Finally, the conclusions are presented in Section 6.

2. Studied Earthquakes and Observations

2.1. Studied Earthquake

In this work, our study focuses on the Luding Ms 6.8 earthquake. The Luding earthquake occurred in Luding County on 5 September 2022, at 12:52 p.m. (UTC+8), and is one of the most significant earthquakes that have occurred in China in recent years [33–35]. Figure 1 indicates the epicenter of the Luding earthquake and the geographic structure of its surrounding areas. Luding County is located in the southwestern part of China's Qinghai–Tibet Plateau region, and is situated at the junction of the major fault zone in the Qinghai–Tibet Plateau and the Sichuan–Yunnan block, serving as a collision zone between the Indian Plate and the Eurasian Plate. Thus, the earthquake activity in this region is relatively frequent, making it a recognized area prone to frequent earthquakes [36].

The Luding earthquake occurred on the left-lateral Moxi Fault Zone at the eastern edge of the Qinghai–Tibet Plateau [37]. This fault zone belongs to the southeastern segment of the Xianshuihe Fault Zone, which exhibits active tectonic activities in the southeastern part of the Qinghai–Tibet Plateau, intersecting with the Longmenshan Fault Zone at this location [37].

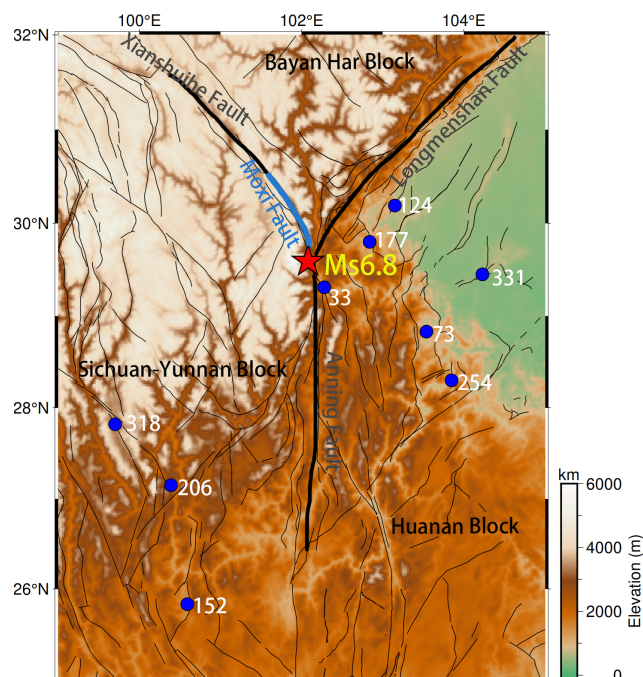


Figure 1. The map shows the tectonic background of western China and the locations of the AETA stations. The red star denotes the Ms 6.8 Luding earthquake, and the blue markers indicate the AETA stations.

2.2. Geomagnetic Observations from AETA

AETA is an integrated software and hardware system capable of acquiring and analyzing earthquake signals in multiple components [38]. Currently, a monitoring network comprising over 220 AETA stations has been established in China, with widespread distribution in the southwestern region of the country [31]. The AETA system collects electromagnetic signals through its electromagnetic sensors. Its operation is based on Faraday’s electromagnetic theory, which obtains induced electromotive force from the vertically varying magnetic field. Subsequently, the signals undergo amplification, filtering, analog-to-digital conversion, and other processing steps [39], yielding ultra-low frequency (ULF) and very low frequency (VLF) electromagnetic signals, with a dynamic range from 0.1 Hz to 10 kHz [40]. The AETA system conducts the final data processing, calculating statistical features such as the mean, variance, skewness, and kurtosis of the raw data [39,41].

In our study, we choose the “magn@abs_mean” dataset provided by the AETA system platform (<http://platform.aeta.cn>, lastest access: 3 November 2023), which provides the data every ten minutes [40]. The identification numbers of the selected stations and their locations are provided in Table 1 and Figure 1. Figure 2 shows the raw magnetic data during the week before the Luding earthquake from the nine stations in this study. For raw magnetic data, preprocessing is required. We first conduct linear interpolation to fill in missing values and normalize the daily sequences. While the data from these stations demonstrate good long-term continuity, they are still disturbed by various non-geological activities. Then, we select the study period from 00:00 a.m. to 06:00 a.m. (UTC+8) each day to avoid the interference caused by human activities and electric power.

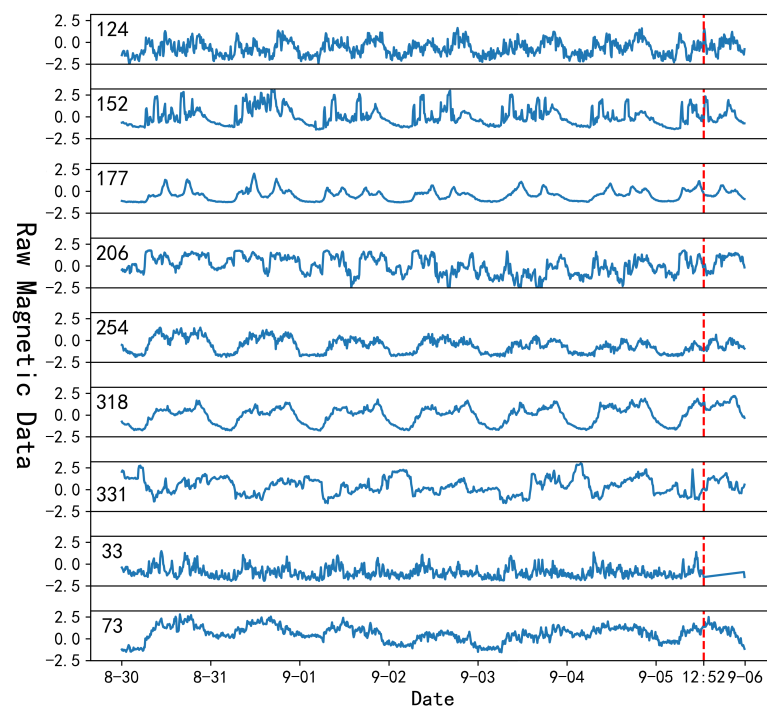


Figure 2. Daily variation of magnetic data (magn@abs_mean) from nine stations. The red dashed line indicates the moment of the Ludian earthquake (2022-09-05 12:52 p.m., UTC+8).

Table 1. Geographical information of the nine AETA stations.

No.	Station ID	Latitude (°N)	Longitude (°E)	Distance from the Epicenter (km)
1	33	29.31	102.28	23.19
2	152	25.83	100.59	184.86
3	73	28.83	103.54	163.42
4	124	30.19	103.15	119.87
5	177	29.80	102.84	84.66
6	318	27.82	99.70	267.21
7	254	28.30	103.85	199.42
8	206	27.15	100.39	195.17
9	331	29.45	104.23	239.10

3. Methods

3.1. Extracting Periodic Components Based on MSSA

Due to the wide spatial impact of earthquakes, conducting a united analysis of geomagnetic data from multiple stations is more reliable than analyzing data from individual stations. To extract the spatial features of geomagnetic data from multiple stations, we consider employing the MSSA method.

MSSA is an extension of Singular Spectrum Analysis (SSA) that incorporates the relationships between multiple time series. It is widely applied to extract periodic components, noise components, and other relevant features from multiple time series data [25,42–45]. SSA is based on singular spectrum decomposition, a powerful technique for decomposing and reconstructing time series [46]. Compared to SSA, MSSA synchronously groups and reconstructs multiple sequences, enabling the simultaneous extraction of sub-sequences with common trends across multiple sequences.

In our study, $x_{n,l}$ is the observational sequence, $n = 1, 2, \dots, N$ and $l = 1, 2, \dots, L$, where n is the number of the N stations in the study area, and L represents the length of the sequence. First, we build a Hankel matrix H with a time lag of m [47],

$$H = \begin{bmatrix} x_{1,1} & x_{1,2} & \cdots & x_{1,L-m+1} \\ x_{1,2} & x_{1,3} & \cdots & x_{1,L-m+2} \\ \vdots & \vdots & \ddots & \vdots \\ x_{1,m} & x_{1,m+1} & \cdots & x_{1,L} \\ x_{2,1} & x_{2,2} & \cdots & x_{2,L-m+1} \\ \vdots & \vdots & \ddots & \vdots \\ x_{2,m} & x_{2,m+1} & \cdots & x_{2,L} \\ \vdots & \vdots & \ddots & \vdots \\ x_{N,1} & x_{N,2} & \cdots & x_{N,L-m+1} \\ \vdots & \vdots & \ddots & \vdots \\ x_{N,m} & x_{N,m+1} & \cdots & x_{N,L} \end{bmatrix} \quad (1)$$

where H is also known as the trajectory matrix, and it is an $(N \times m) \times (L - m + 1)$ matrix. m represents the length of this sliding window, which is also called the time delay window or the embedding window. The function of the time delay window is to balance the time–frequency domain resolution [47]. Generally speaking, the larger the m , the higher the frequency domain resolution, and the more obvious the extracted low-frequency components. Conversely, the high-frequency component is more significant. The value of m directly affects the size of the trajectory matrix H . In our study, we set the values of N , L , and m as 9, 37, and 3, respectively. Here, $N = 9$ for 9 stations. $L = 37$ indicates the length of each magnetic data sequence (00:00 a.m. to 06:00 a.m.). Generally, m does not exceed 1/4 of the length of the sequence. m is finally set to 3, which can extract clear low-frequency components while ensuring low computational reconstruction.

Next, we conduct a Singular Value Decomposition (SVD) on matrix H , $H = U\Lambda V^T$, where the matrices U and V represent the left and right singular matrices, respectively. Λ is a diagonal matrix with r singular values λ_k for $k = 1, 2, \dots, r$, arranged in descending order, where

$$r = \begin{cases} N \times m, & N \times m \leq L - m + 1 \\ L - m + 1, & L - m + 1 < N \times m \end{cases} \quad (2)$$

Then, the eigen sub-sequence T_k corresponding to λ_k , can be obtained, $T_k = \sqrt{\lambda_k} u_k v_k^T$, where the column vectors u_k and v_k are sourced from the matrices U and V , respectively [25]. The reconstructed sub-sequences $R_{n,l}^{(k)}$, which corresponds to T_k , are derived by applying diagonal averaging to T_k

$$R_{n,l}^{(k)} = \begin{cases} \frac{1}{l} \sum_{i=1}^l T_{i,l-i+1}, & 1 \leq l < m \\ \frac{1}{m} \sum_{i=1}^m T_{i,l-i+1}, & m \leq l < N - m + 1 \\ \frac{1}{L-l+1} \sum_{i=l-L+m}^m T_{i,l-i+1}. & N - m + 1 \leq l < L \end{cases} \quad (3)$$

For each station, we use a short form for $R_{n,l}^{(k)}$ as RC_k , where $RC_k = R_{n,l}^{(k)}$ [47]. Since the singular values in the diagonal matrix Λ are arranged in descending order, the reconstructed sub-sequence RC_k corresponding to the singular value λ_0 is the most significant in terms of contribution, indicating the primary low-frequency periodic component in

the reconstructed sequence. Therefore, in this study, we consider RC_0 to be the magnetic periodic low-frequency component.

Figure 3a,b present two examples of the reconstructed component signals for nine stations with a time lag window $m = 3$. Figure 3a shows the MSSA reconstruction results for a normal case. The first row displays the variations in geomagnetic raw data for these nine stations over three consecutive days (00:30 a.m. to 04:30 a.m. each day). The second row shows the reconstructed geomagnetic periodic component RC_0 for each station. The last row presents the other components corresponding to relatively small singular values $\sum_{k=1}^{26} RC_k$, which may contain some high-frequency geomagnetic changes and noises. Figure 3b shows the reconstruction results for an earthquake period. As we can see, what accounts for the highest contribution in the daily geomagnetic data is the daily periodic and low-frequency components. It can be noticed that, after MSSA, the periodicity of each station can be seen very clearly, even if it is not prominent in the raw data. Therefore, we want to investigate whether there is any earthquake-related information in this component. As shown in Figure 3a, for a normal state, the daily periodic low-frequency components for each station should be very similar. For an abnormal state as shown in Figure 3b, there are some changes and differences in their daily periodic low-frequency components. Thus, we expect that the MSSA can extract the daily periodic low-frequency component for multi-stations and capture the changes in those components.

3.2. Building a Geomagnetic Topology Network for the Periodic Components

Topology networks are commonly used to represent an observational network [27,29]. To assess the overall relationship across multiple stations, we construct a geomagnetic topology network G for geomagnetic periodic component observations, with $G = (S, E)$, where S is a set of nodes $S = [s_1, s_2, \dots, s_N]$. Here, the AETA stations are represented as the nodes. E is the set of the network edges, expressed as the connectivity between nodes. The structure and properties of topology networks are studied through graph theory, regardless of the actual geographical environment and the distance between stations. We design this topology network G as a weight-free network, so all edges are of equal weight, and the matrix E is shown below:

$$E = \begin{bmatrix} e_{1,1} & e_{1,2} & \cdots & e_{1,N} \\ e_{2,1} & e_{2,2} & \cdots & e_{2,N} \\ \vdots & \vdots & \ddots & \vdots \\ e_{N,1} & e_{N,2} & \cdots & e_{N,N} \end{bmatrix} \tag{4}$$

where $e_{i,j}$ represents an edge between the nodes s_i and s_j , taking values of 1 or 0 to indicate the presence or absence of the connectivity between the stations,

$$e_{i,j} = \begin{cases} 1, & |p_{i,j}| \geq 0.8 \\ 0, & |p_{i,j}| < 0.8 \end{cases} \tag{5}$$

where $p_{i,j}$ represents the Pearson correlation coefficient between the two RC_0 s, $RC_{0(i,l)}$ and $RC_{0(j,l)}$, from station i and station j , for $i, j \in N, l = 1, 2, \dots, L$, defined as follows:

$$p_{i,j} = \frac{cov(RC_{0(i,l)}, RC_{0(j,l)})}{\sigma_{RC_{0(i,l)}} \sigma_{RC_{0(j,l)}}} = \frac{\sum_{l=1}^L (RC_{0(i,l)} - \overline{RC_{0(i,l)}})(RC_{0(j,l)} - \overline{RC_{0(j,l)}})}{\sqrt{\sum_{l=1}^L (RC_{0(i,l)} - \overline{RC_{0(i,l)}})^2 (RC_{0(j,l)} - \overline{RC_{0(j,l)}})^2}} \tag{6}$$

where $cov(X, Y)$ represents the covariance between sequences X and Y , σ_X represents the standard deviations of sequences X , and \overline{X} represents the mean of sequences X .

Then, we set a threshold value to quantify each $p_{i,j}$. Generally, a Pearson correlation coefficient greater than 0.8 between two sequences indicates a strong linear relationship between them. Therefore, we set this threshold to 0.8 as indicated by the quantification criterion in Equation (5).

To further evaluate the significance of the overall connectivity of the network, we define the network centrality [48] as

$$\bar{k} = \frac{1}{N(N-1)} \sum_{i=1}^N \sum_{j=1}^N e_{i,j}, j \neq i \quad (7)$$

The value of \bar{k} represents the correlations of multiple geomagnetic stations. Here, we provide two examples to show the connections in a topology network. Figure 3c shows a fully connected topology network on 14 August 2022. As we can see, all nodes are connected, which means that the magnetic periodic components of the nine stations are strongly similar to each other as shown in Figure 3a. In this case, the whole connection matrix E will be a full one matrix, that is, all $e_{i,j} = 1$; Figure 3d represents the topology network on the day of the Luding earthquake, and there is no connection between some nodes, i.e., their corresponding $e_{i,j} = 0$. This represents the absolute value of the correlation coefficients between the magnetic periodic components of the corresponding station as being less than 0.8, and they are not strongly consistent as shown in Figure 3b.

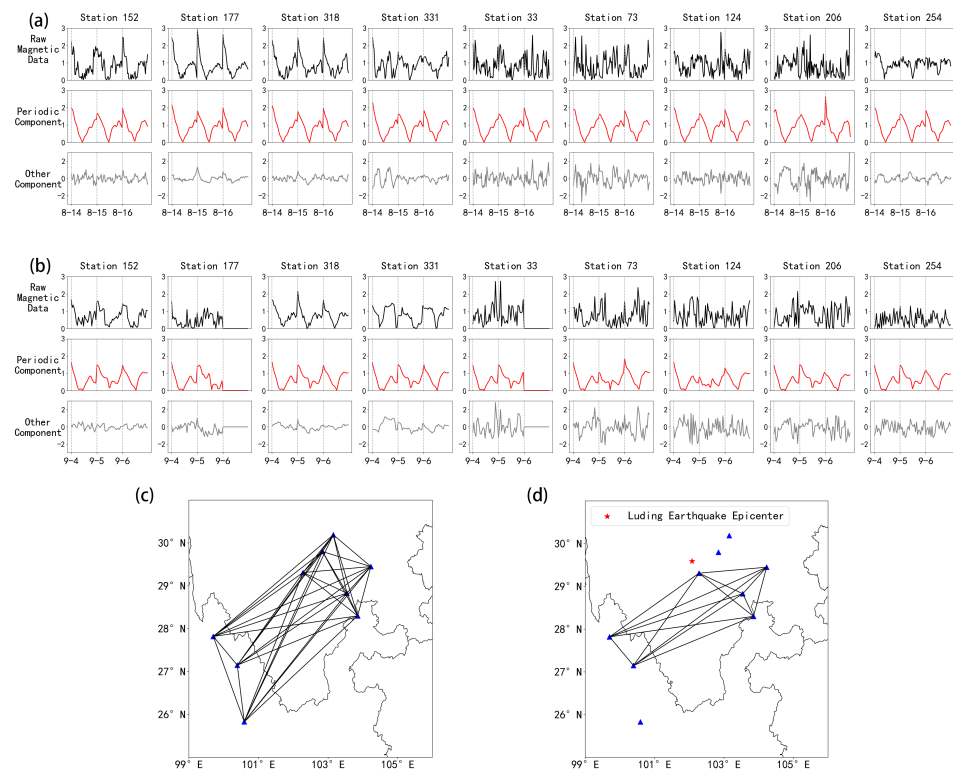


Figure 3. (a) An example of MSSA reconstruction results for a normal case. There are variations in magnetic data from 9 stations along with their periodic and other components from August 14 to August 16 (seismic quiet period). The black lines indicate the raw magnetic data, and the red and grey lines represent the periodic components and other components of geomagnetic observations, respectively. (b) An example of MSSA reconstruction results for an earthquake period. There are variations of the periodic and other components from September 4 to September 6. The Luding earthquake occurred on 5 September 2022. (c) A fully connected topology network on 14 August 2002, corresponding to (a). The blue triangles represent the AETA stations. (d) The topology network on the day of the Luding earthquake.

3.3. Excluding the Anomalous Interference from One Single Station

In general, RC_0 is capable of reflecting changes in the periodic components [49]. In this study, we focus on the overall relationship between the periodic components of multiple stations. However, for a united analysis of multiple stations, an outlier caused by accidental factors at one station can affect the entire network connectivity. Thus, to identify and

eliminate unreliable RC_0 from one particular single station, we need to evaluate whether RC_0 at a given station is significantly different from all other stations.

We utilize K-means clustering to classify RC_0 into two classes: $M1$ and $M2$. Here, the class with fewer stations is called the isolated class $M1$, and the $M2$ with more stations is the mainstream class. When the clustering result shows that the $M1$ class contains only one station, we consider the data of this station to have been influenced by accident factors and as needing to be removed. To find the situation of only one station in $M1$, we first initialize the clustering centers μ_1 and μ_2 for two classes. Then, we calculate the Euclidean distance, $d_{i,j} = |C_{RCi} - \mu_j|$ for $i = 1, 2, \dots, N$ and $j = 1, 2$; C_{RCi} is the object of our clustering. Subsequently, each C_{RCi} is assigned to the class corresponding to the closest clustering center based on the magnitude of $d_{i,1}$ and $d_{i,2}$. Once all points are classified, the clustering centers are updated, and this process is iterated until the difference in clustering centers between two consecutive iterations is less than 10^{-4} . The final classification result is obtained through this iterative procedure.

In this study, we set $C_{RC} = [C_{RC1}, C_{RC2}, \dots, C_{RCN}]$, in which C_{RCi} represents the correlation of the RC_0 of station i with the RC_0 s of all other stations. If the RC_0 of station i significantly deviates from that of the other stations, its corresponding C_{RCi} will be very small, leading it to be classified as an isolated class. Therefore, the RC_0 of the single anomalous station can be identified and removed.

Figure 4 demonstrates three possible cases of the clustering results. Figure 4a depicts an example of the normal clustering results, the elements of set C_{RC} are roughly uniformly distributed among two classes, where the black crosses represent the cluster centers, while the red and green points represent the points in the two classes. Figure 4b is a typical clustering result with one outlier belonging to one class. In this case, the clustering centers are farther apart. Thus, we can recognize that outlier and remove it. Figure 4c shows there are two or more outlier stations; we do not consider these outliers to be accidental disturbances and therefore do not address them. Moreover, this case is very likely to be extracted as a network anomaly.

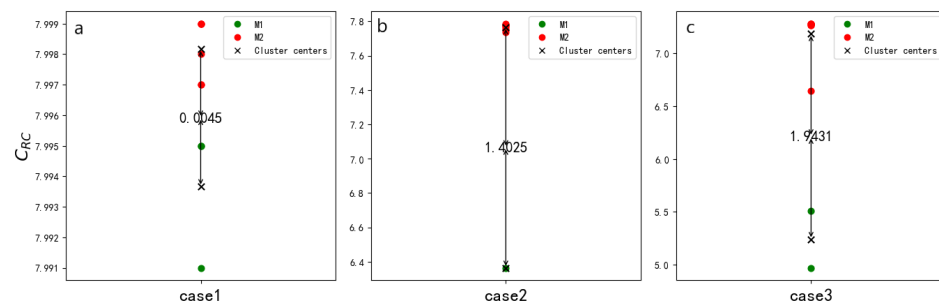


Figure 4. An example of three possible cases of clustering results. (a) The absence of any anomalous RC_0 data. (b) One of the classes is one single outlier. (c) One of the classes is two or more outliers.

4. Results

To investigate the correlation of geomagnetic observations between multiple stations preceding the Luding earthquake, we construct a geomagnetic topology network consisting of nine AETA stations within a 500-kilometer radius from the epicenter by utilizing the aforementioned method. The daily geomagnetic topology network from 20 days before to 5 days after the Luding earthquake is shown in Figure 5. It can be found that, in the first 10 days, the network is basically fully connected, which means that there is very high consistency in the periodic components over the nine stations. Then, the connectivity of the network is gradually weakened from 30 August to 2 September 2022. On the day of the earthquake, the connectivity of the network reaches its lowest level and remains a weak connection for 5 days after the earthquake. It is important to note that, to avoid daytime interference, we study the geomagnetic data from 0:00 a.m. to 4:30 a.m. To be precise, the network showing on the day of the earthquake also precedes the earthquake (12:52 p.m.).

Next, we examine the network centrality \bar{k} , spanning 45 days before and 15 days after the earthquake, and the result is shown in Figure 6. The threshold of 0.949 is the mean of centrality minus two times the standard deviation from 2017 to 2022. As we can see, there are several values of centrality dropping from a normal value of 1 to a small value before the earthquake, which indicates a weakened correlation between the geomagnetic periodic components of the nine stations. Subsequently, we notice that the centrality anomaly of four consecutive days from 30 August to 2 September appears before the earthquake. The value of centrality drops from 1 to 0.93 to 0.79, and finally to 0.62. Especially on the days of the earthquake, the centrality reaches its minimum value within these 60 days. Finally, within 10 days after the earthquake, the overall trend of \bar{k} shows a recovery sign. In addition, these results are consistent with the network of Figure 5. Therefore, we consider that our results may suggest a correlation between centrality anomalies and the earthquake event. At the beginning of August, we also observe several centrality anomalies. However, these anomalies are of discontinuity and one-day duration, as well as a nearly one-month interval with the earthquake. It is possible that these centrality anomalies are not related to the earthquake.

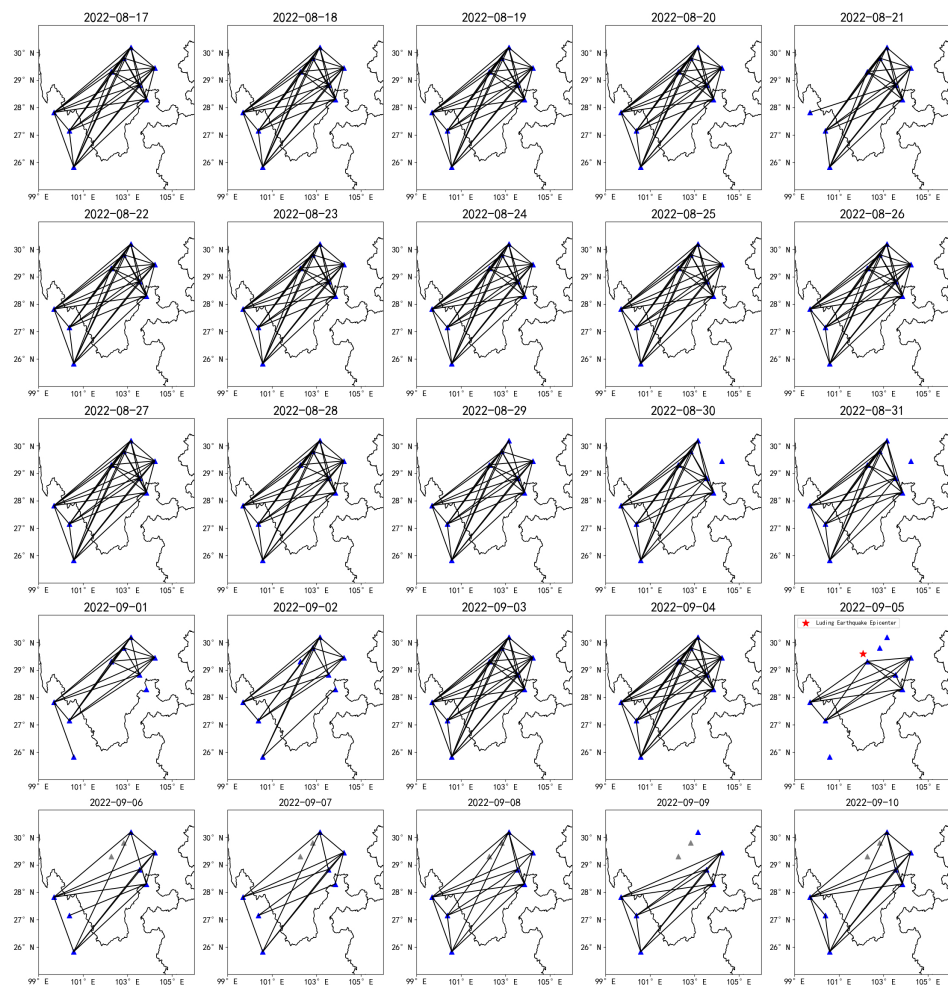


Figure 5. Daily geomagnetic topology network diagram from 20 days before to 5 days after the Luding earthquake. The black lines indicate the edges between two stations, the blue triangles represent the AETA stations, and the red star denotes the epicenter of the Luding earthquake. It is noted that the data from stations 33 and 177 (in grey) are completely missing for several days following the Luding earthquake, so we do not consider their nodal connectivity during this period.

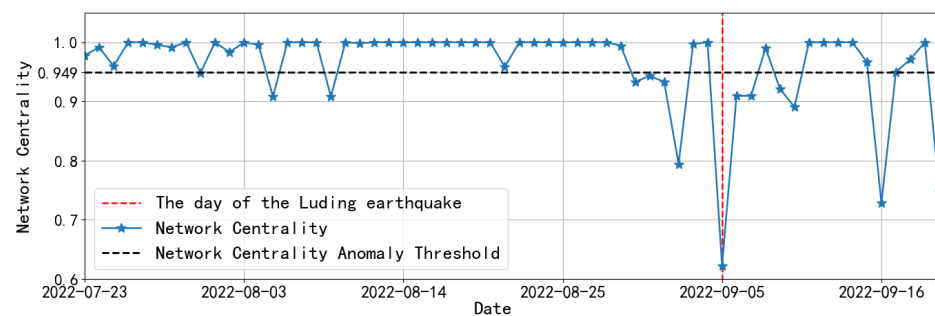


Figure 6. The variations of network centralities for the Luding earthquake. The blue line represents the network centrality from 45 days before to 15 days after the Luding earthquake. The red dashed line marks the date of the Luding earthquake.

5. Discussion

5.1. Network Centrality during Random Periods

To further explore the possibility of the extracted Luding earthquake-related anomalies from network centrality in the geomagnetic network, we randomly select two additional periods before the Luding earthquake. These periods are characterized by a low occurrence of earthquakes within the network and relatively small magnitudes of earthquake events. They are 1 September 2021, to 30 October 2021, and 1 April 2022, to 30 May 2022. For each of the periods, we employ the same methodology to calculate the network centrality. The changes in the network centrality are shown in Figure 7.

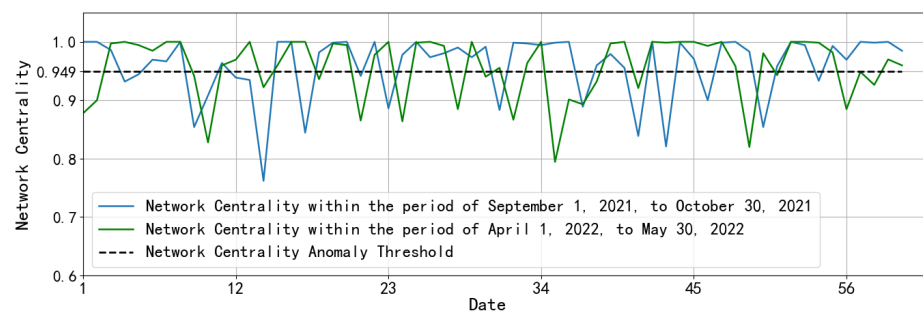


Figure 7. Network centralities for two random periods.

It is evident that the centrality anomalies for the random periods in the geomagnetic topology network are relatively messy and disordered. The result implies that during periods characterized by fewer earthquake events and lower magnitudes, the network centrality values do not display significant anomalies. Thus, this finding supports the correlation between the extracted network anomalies in Section 4 and the Luding earthquake.

5.2. Network Centrality for an Additional Network

To further assess the spatial sensitivity of the extracted anomalies associated with the Luding earthquake, we construct a new geomagnetic network using seventeen additional stations located outside the original network; the geographical locations are presented in Table 2 and Figure 8b. Although the epicenter distance is larger for each station, the coverage of the additional network is a much larger area. We repeat the above method in Section 3 for the additional network and calculate its network centrality. The changes in the network centrality are shown in Figure 8c.

Figure 8c illustrates that the additional network exhibits higher fluctuations and stronger amplitudes. Multiple anomalies in the network centrality appear approximately 45 days to 5 days before the earthquake, especially on August 16 and 29. Furthermore, on the day of the Luding earthquake, although the centrality anomaly is not so pronounced compared to other periods, there is a recognizable decrease in network centrality.

These results can be attributed to two factors. Firstly, the presence of several farther stations introduces more randomness and external interference; the additional network may be influenced by other earthquake events with medium magnitudes within its extended coverage area. Therefore, the expanded coverage weakens the correlation of geomagnetic periodic components among the stations. As a result, the network centrality fluctuates more. Secondly, the coverage of the additional network is inclusive of both the epicenter and the original network, so the network centralities also appear as suspected anomalies for the Luding earthquake. In the studied 60 days, the values of the centrality anomalies grow stronger in the pre-earthquake period and recover after the earthquake. However, the confidence of the centrality anomalies in the additional network still needs to be explored further.

Table 2. Geographical information of the additional AETA stations.

No.	Station ID	Latitude (°N)	Longitude (°E)	Distance from the Epicenter (km)
1	50,117	24.12	102.75	611
2	146	32.59	105.23	448
3	332	23.73	102.52	653
4	106	24.44	98.59	668
5	24	32.63	105.75	486
6	155	32.78	105.42	476
7	161	23.38	103.16	698
8	220	24.47	102.62	571
9	186	25.11	99.12	577
10	226	32.93	104.69	446
11	113	32.44	105.35	444
12	115	25.03	98.52	616
13	141	33.15	104.2	444
14	183	25.21	98.49	602
15	43	24.95	98.43	629
16	172	23.37	102.38	692
17	202	23.23	102.84	711

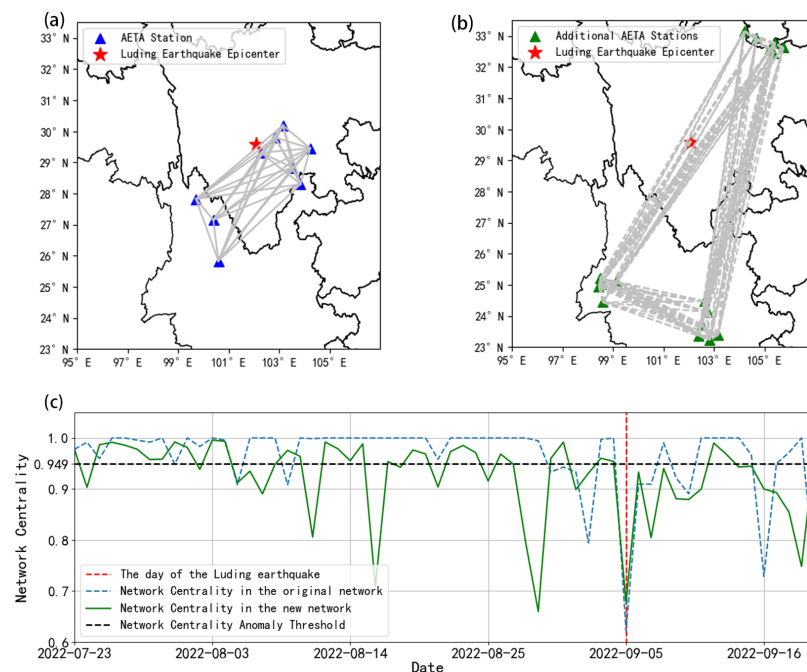


Figure 8. (a) Distribution map of the original network. The blue triangles represent the stations of the original network, and the solid gray lines are the connections between stations. (b) Distribution map of the additional network. The green triangles represent the stations of the additional network, and the dotted gray lines are the connections between stations. (c) The network centrality of the original and additional networks during the 45 days before and 15 days after the Luding earthquake. The blue dashed line represents the network centrality of the original network, while the green line represents the network centrality of the additional network.

By comparing the centrality anomalies in the original and additional networks for the Luding earthquake, it becomes evident that the original geomagnetic topology network sensitively captures the daily variations in the overall correlation of geomagnetic periodic components, demonstrating that the original network effectively extracts the spatial anomalies associated with the Luding earthquake.

5.3. Superposed Epoch Analysis (SEA) for the Geomagnetic Topology Network

To further validate the efficiency of the geomagnetic topology network for other earthquakes, we conduct a statistical study using the Superposed Epoch Analysis (SEA) from 2008 to 2022 [50]. SEA unveils temporal patterns and trends surrounding specific events, thereby offering insights into their impact and underlying relationships [51–54].

Initially, we create circles with a radius of 100 kilometers, centered at each station of our geomagnetic topology network. Then, the externally located circles by their common tangential points are connected to define our statistical region. Thus, the earthquakes with magnitudes greater than 5 in this range are our target earthquakes. AETA provides the observations from 2017, so we utilize the geomagnetic data from the China Earthquake Networks Center to study the earthquakes before 2017. This study is authorized for data from 2008 to 2014. To ensure consistency in the studied region, we choose eight stations to construct the geomagnetic topology network; their locations are listed in Table 3. The studied earthquakes and the constructed networks are shown in Figure 9.

Table 3. Geographical information of the stations from China Earthquake Networks Center.

No.	Station ID	Latitude (°N)	Longitude (°E)	Distance from the Epicenter (km)
1	CDP	103.76	30.91	218
2	NNS	102.609	27.221	268
3	CHX	101.53	25.032	509
4	YOS	100.768	26.695	346
5	MUL	101.272	27.932	200
6	XIC	102.55	27.89	194
7	WEC	101.646	27.454	241
8	NAS	101.69	26.54	341

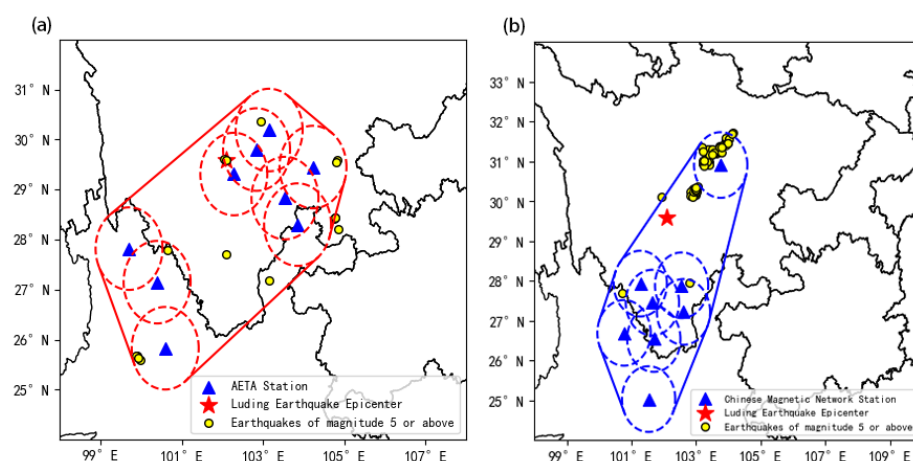


Figure 9. (a) The outermost red line represents the statistical region of the geomagnetic topology network, and the yellow dots indicate the target earthquakes from 2018 to 2022. The blue triangle represents the AETA station. (b) The outermost blue line represents the statistical region of the geomagnetic topology network, and the yellow dots indicate the target earthquakes from 2008 to 2014. The blue triangle represents the Chinese Magnetic networks station.

Next, we perform the SEA for the target earthquakes [55]. We calculate the network centrality for these earthquakes within the 45 days preceding each earthquake and the 15 days following them. The threshold for determining centrality anomaly remains at 0.949. If one day exhibits a centrality anomaly, we increment the count by one for that specific day across the entire dataset [55]. In the analysis from 2018 to 2022, we employ this procedure for 65 target earthquakes with magnitude greater than 4, followed by superposing the counts across all datasets. Since there are fewer than 10 earthquakes of magnitude five or greater, it is not statistical. Similarly, in the analysis from 2008 to 2014, we repeat this procedure for 20 target earthquakes with magnitudes greater than 5. The SEA results of one-day counts and five-day counts are shown in Figure 10. To further assess statistical significance, we randomly select 65 days within the complete dataset spanning from 2018 to 2022, excluding the dates coinciding with earthquake events, and apply the same procedure. And the same operation is implemented for the data from 2008 to 2014. We repeat this random SEA test 10,000 times to calculate the mean and standard deviation [50].

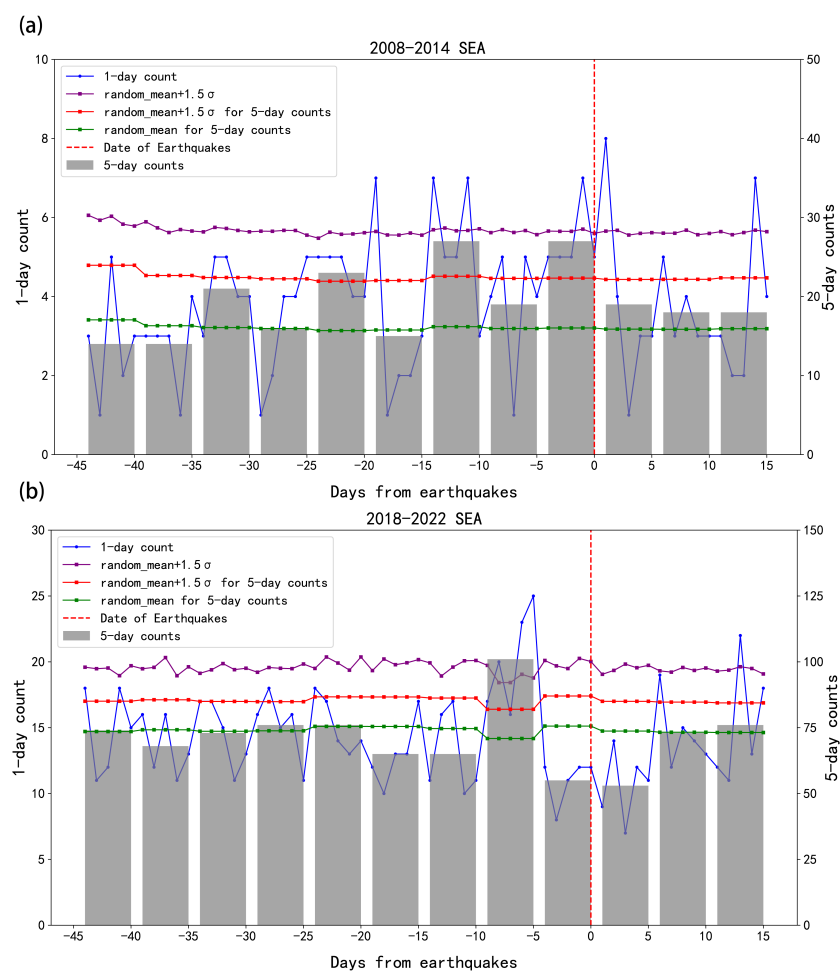


Figure 10. (a) The SEA results of geomagnetic disturbance observation network centrality from 2008 to 2014. (b) The SEA results of geomagnetic disturbance observation network centrality from 2018 to 2022.

Assuming no correlation between centrality (\bar{k}) anomalies and earthquake events, the anomaly counts for these actual earthquakes would be expected to roughly follow the random distribution. This also implies that if the counts for one day or five days exceed the random mean plus 1.5 standard deviation level, it indicates a statistically significant correlation between the earthquakes and centrality anomalies. Figure 10a indicates that within the 20 days preceding the earthquakes, there are four one-day anomaly counts, surpassing the level of mean plus 1.5 times the standard deviation. Moreover, the five-day anomaly counts exceed its mean plus 1.5 times the standard deviation for -15 to -10 days

and -5 to 0 days. Figure 10b indicates both the one-day anomaly counts and the five-day anomaly counts from -10 to -5 days before the earthquake exceeds the mean plus 1.5 times the standard variance. These results highly indicate the correlation between earthquakes and centrality anomalies.

In addition to geomagnetic data, significant progress has been made in investigating the precursors associated with the Luding earthquake over the past two years [11]. Wu et al. [56] analyzed the variations of the atmospheric electric field (AEF) in the 15 days leading up to the Luding earthquake. They investigated the observed AEF anomalies and concluded that four negative AEF anomalies are likely associated with the Luding earthquake. Zhu et al. [57] studied the outgoing longwave radiation (OLR) data prior to the Luding earthquake. Significant OLR anomalies were detected on August 9, August 18, and August 28 before the Luding earthquake. Liu et al. [58] also investigated the anomalies in AEF and OLR before the Luding earthquake, along with examining disturbances in the ionosphere and investigating the anomalies in infrared radiation and hot spring ions. They found that the AEF anomalies appeared approximately one week before the earthquake, the (infrared brightness temperature) IBT anomalies showed throughout August, and the anomalies in hot spring ions appeared in July and lasted until September, which may indicate the enhanced seismic-ionospheric coupling effect. Then, we further exhibit a summary of the anomalies of different observations as shown in Figure 11.

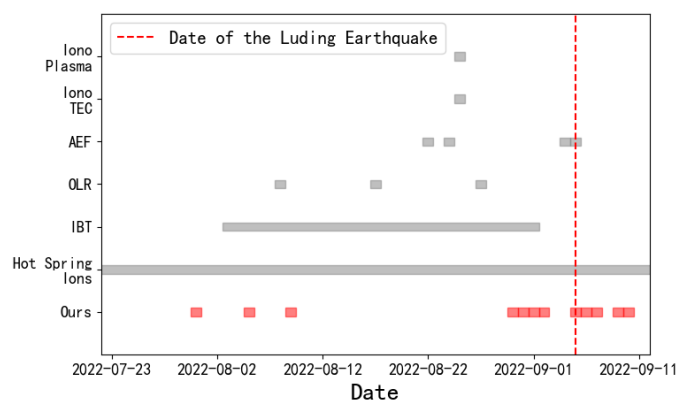


Figure 11. A summary of the geomagnetic anomalies in our study (in red) and the anomalies of different observations (in gray) associated with the Ms 6.8 Luding Earthquake [56–58].

In Figure 11, the multiple observational parameters show anomalies during the 45 days before the earthquake, but these anomalies appear at different times. Since different methods are designed with different principles for different features, it is reasonable that different features appear at different times. Therefore, developing a method that can recognize multiple features is important and challenging.

6. Conclusions

In this study, we employ the MSSA method to reconstruct the periodic components of geomagnetic data from multiple stations. Based on the correlation of the periodic components, we establish a geomagnetic topology network and calculate the network centrality. The network centrality quantifies the connectivity of the geomagnetic topology network, reflecting the overall correlation between the geomagnetic data from multiple stations. Subsequently, we investigate the changes in network centrality around the Luding earthquake on 5 September 2022. We extracted several centrality anomalies during the studied period. Especially in the 6 to 3 days and hours before the earthquake, the centrality drops from 1 to 0.93 to 0.79, and finally to 0.62. Then, we further examine the extracted anomalies in both time and space, demonstrating the significance of the centrality anomalies for the Luding earthquake. Additionally, we compile the counts of centrality anomalies during 2008–2022 through the SEA method. For the statistical SEA results of more than 80 earthquakes, we

find that centrality anomalies are more likely to occur before an earthquake than afterward. Our method unites information from multiple geomagnetic stations and effectively extracts spatial features between multiple stations, as well as providing a new method of earthquake precursor analysis of ground-based observation data.

Author Contributions: Conceptualization, Z.Y.; methodology, Z.Y.; software, Z.Y., and X.J.; validation, X.J., and X.W.; formal analysis, Z.Y., X.J., X.W. and C.C.; investigation, Z.Y.; resources, Z.Y.; data curation, Z.Y.; writing—original draft preparation, Z.Y., X.J., C.C. and H.Z.; writing—review and editing, Z.Y., X.J. and H.Z.; supervision, Z.Y. and H.Z. All authors have read and agreed to the published version of the manuscript.

Funding: This work was supported by the National Natural Science Foundation of China (Nos. 42204005 and 62171421), the Natural Science Foundation of Shandong Province (No. ZR2022QF130), the TaiShan Scholars Youth Expert Program of Shandong Province (No. tsqn202306096), and the Hainan Provincial Natural Science Foundation of China (No. 622RC669).

Data Availability Statement: The geomagnetic data and the earthquake catalogs can be downloaded from China Earthquake Networks Center, National Earthquake Data Center (<http://data.earthquake.cn>, latest access: 17 October 2021). The AETA data can be downloaded from the website: <https://platform.aeta.cn/zh-CN/competitionpage/download> (latest access: 3 November 2023).

Acknowledgments: Acknowledgment for the geomagnetic data support from China Earthquake Networks Center, and National Earthquake Data Center. The authors would like to thank Zhang, Xiuqin from the China Earthquake Administration for the invaluable assistance in accessing the websites as well as downloading the geomagnetic data. The authors would also like to thank the AETA platform.

Conflicts of Interest: The authors declare no conflicts of interest.

References

1. Akhoondzadeh, M.; De Santis, A.; Marchetti, D.; Wang, T. Developing a Deep Learning-Based Detector of Magnetic, Ne, Te and TEC Anomalies from Swarm Satellites: The Case of Mw 7.1 2021 Japan Earthquake. *Remote Sens.* **2022**, *14*, 1582. [[CrossRef](#)] [[CrossRef](#)]
2. Xiong, P.; Zhai, D.; Long, C.; Zhou, H.; Zhang, X.; Shen, X. Long short-term memory neural network for ionospheric total electron content forecasting over China. *Space Weather.* **2021**, *19*, e2020SW002706. [[CrossRef](#)] [[CrossRef](#)]
3. Chen, H.; Han, P.; Hattori, K. Recent Advances and Challenges in the Seismo-Electromagnetic Study: A Brief Review. *Remote Sens.* **2022**, *14*, 5893. [[CrossRef](#)] [[CrossRef](#)]
4. Hattori, K.; Han, P.; Yoshino, C.; Febriani, F.; Yamaguchi, H.; Chen, C.H. Investigation of ULF seismo-magnetic phenomena in Kanto, Japan during 2000–2010: Case studies and statistical studies. *Surv. Geophys.* **2013**, *34*, 293–316. [[CrossRef](#)] [[CrossRef](#)]
5. Marchetti, D.; De Santis, A.; Campuzano, S.A.; Zhu, K.; Soldani, M.; D’Arcangelo, S.; Orlando, M.; Wang, T.; Cianchini, G.; Di Mauro, D.; et al. Worldwide statistical correlation of eight years of swarm satellite data with M5. 5+ earthquakes: New hints about the preseismic phenomena from space. *Remote Sens.* **2022**, *14*, 2649. [[CrossRef](#)] [[CrossRef](#)]
6. Parrot, M.; Tramutoli, V.; Liu, T.J.; Pulinets, S.; Ouzounov, D.; Genzano, N.; Lisi, M.; Hattori, K.; Namgaladze, A. Atmospheric and ionospheric coupling phenomena associated with large earthquakes. *Eur. Phys. J. Spec. Top.* **2021**, *230*, 197–225. [[CrossRef](#)] [[CrossRef](#)]
7. Pulinets, S.; Ouzounov, D. Lithosphere–Atmosphere–Ionosphere Coupling (LAIC) model—An unified concept for earthquake precursors validation. *J. Asian Earth Sci.* **2011**, *41*, 371–382. [[CrossRef](#)] [[CrossRef](#)]
8. Li, M.; Lu, J.; Zhang, X.; Shen, X. Indications of Ground-based Electromagnetic Observations to A Possible Lithosphere–Atmosphere–Ionosphere Electromagnetic Coupling before the 12 May 2008 Wenchuan MS 8.0 Earthquake. *Atmosphere* **2019**, *10*, 355. [[CrossRef](#)] [[CrossRef](#)]
9. Sarlis, N.V. Statistical significance of earth’s electric and magnetic field variations preceding earthquakes in Greece and Japan revisited. *Entropy* **2018**, *20*, 561. [[CrossRef](#)] [[CrossRef](#)]
10. Zhang, Y.; Li, M.; Huang, Q.; Shao, Z.; Liu, J.; Zhang, X.; Ma, W.; Parrot, M. Statistical correlation between DEMETER satellite electronic perturbations and global earthquakes with $M \geq 4.8$. *IEEE Trans. Geosci. Remote Sens.* **2023**. [[CrossRef](#)] [[CrossRef](#)]
11. Chen, C.H.; Zhang, S.; Mao, Z.; Sun, Y.Y.; Liu, J.; Chen, T.; Zhang, X.; Yisimayili, A.; Qing, H.; Luo, T.; et al. The Lithosphere–Atmosphere–Ionosphere Coupling of Multiple Geophysical Parameters Approximately 3 Hours Prior to the 2022 M6.8 Luding Earthquake. *Geosciences* **2023**, *13*, 356. [[CrossRef](#)]
12. Pulinets, S.; Tsidilina, M.; Ouzounov, D.; Davidenko, D. From Hector Mine M7. 1 to Ridgecrest M7. 1 earthquake. A look from a 20-year perspective. *Atmosphere* **2021**, *12*, 262. [[CrossRef](#)]

13. Pulinets, S.; Davidenko, D. The nocturnal positive ionospheric anomaly of electron density as a short-term earthquake precursor and the possible physical mechanism of its formation. *Geomagn. Aeron.* **2018**, *58*, 559–570. [[CrossRef](#)]
14. Pulinets, S.; Gaivoronska, T.; Leyva Contreras, A.; Ciralo, L. Correlation analysis technique revealing ionospheric precursors of earthquakes. *Nat. Hazards Earth Syst. Sci.* **2004**, *4*, 697–702. [[CrossRef](#)]
15. Liu, Q.; De Santis, A.; Piscini, A.; Cianchini, G.; Ventura, G.; Shen, X. Multi-parametric climatological analysis reveals the involvement of fluids in the preparation phase of the 2008 Ms 8.0 wenchuan and 2013 Ms 7.0 lushan earthquakes. *Remote Sens.* **2020**, *12*, 1663. [[CrossRef](#)]
16. Han, P.; Zhuang, J.; Hattori, K.; Chen, C.H.; Febriani, F.; Chen, H.; Yoshino, C.; Yoshida, S. Assessing the potential earthquake precursory information in ULF magnetic data recorded in Kanto, Japan during 2000–2010: Distance and magnitude dependences. *Entropy* **2020**, *22*, 859. [[CrossRef](#)] [[CrossRef](#)]
17. Han, P.; Hattori, K.; Zhuang, J.; Chen, C.H.; Liu, J.Y.; Yoshida, S. Evaluation of ULF seismo-magnetic phenomena in Kakioka, Japan by using Molchan's error diagram. *Geophys. J. Int.* **2016**, *208*, 182–490. [[CrossRef](#)] [[CrossRef](#)]
18. Potirakis, S.; Karadimitrakis, A.; Eftaxias, K. Natural time analysis of critical phenomena: The case of pre-fracture electromagnetic emissions. *Chaos Interdiscip. J. Nonlinear Sci.* **2013**, *23*. [[CrossRef](#)] [[CrossRef](#)]
19. Chen, H.J.; Chen, C.C. Testing the correlations between anomalies of statistical indexes of the geoelectric system and earthquakes. *Nat. Hazards* **2016**, *84*, 877–895. [[CrossRef](#)] [[CrossRef](#)]
20. Guo, Q.; Yong, S.; Wang, X. Statistical analysis of the relationship between AETA electromagnetic anomalies and local earthquakes. *Entropy* **2021**, *23*, 411. [[CrossRef](#)] [[CrossRef](#)]
21. Rundle, J.; Tiampo, K.; Klein, W.; Sa Martins, J. Self-organization in leaky threshold systems: The influence of near-mean field dynamics and its implications for earthquakes, neurobiology, and forecasting. *Proc. Natl. Acad. Sci. USA* **2002**, *99*, 2514–2521. [[CrossRef](#)]
22. Wen, S.; Chen, C.H.; Yen, H.Y.; Yeh, T.K.; Liu, J.Y.; Hattori, K.; Peng, H.; Wang, C.H.; Shin, T.C. Magnetic storm free ULF analysis in relation with earthquakes in Taiwan. *Nat. Hazards Earth Syst. Sci.* **2012**, *12*, 1747–1754. [[CrossRef](#)]
23. Golyandina, N.; Nekrutkin, V.; Zhigljavsky, A.A. *Analysis of Time Series Structure: SSA and Related Techniques*; CRC Press: Boca Raton, FL, USA, 2001.
24. Guo, J.; Li, W.; Chang, X.; Zhu, G.; Liu, X.; Guo, B. Terrestrial water storage changes over Xinjiang extracted by combining Gaussian filter and multichannel singular spectrum analysis from GRACE. *Geophys. J. Int.* **2018**, *213*, 397–407. [[CrossRef](#)] [[CrossRef](#)]
25. Yu, Z.; Hattori, K.; Zhu, K.; Chi, C.; Fan, M.; He, X. Detecting earthquake-related anomalies of a borehole strain network based on multi-channel singular spectrum analysis. *Entropy* **2020**, *22*, 1086. [[CrossRef](#)] [[CrossRef](#)]
26. Martinetz, T.; Schulten, K. Topology representing networks. *Neural Netw.* **1994**, *7*, 507–522. [[CrossRef](#)] [[CrossRef](#)]
27. Abe, S.; Suzuki, N. Small-world structure of earthquake network. *Phys. A Stat. Mech. Its Appl.* **2004**, *337*, 357–362. [[CrossRef](#)] [[CrossRef](#)]
28. Jiménez, A.; Tiampo, K.; Posadas, A. Small world in a seismic network: the California case. *Nonlinear Process. Geophys.* **2008**, *15*, 389–395. [[CrossRef](#)] [[CrossRef](#)]
29. Chorozoglou, D.; Kugiumtzis, D.; Papadimitriou, E. Application of complex network theory to the recent foreshock sequences of Methoni (2008) and Kefalonia (2014) in Greece. *Acta Geophys.* **2017**, *65*, 543–553. [[CrossRef](#)] [[CrossRef](#)]
30. Lv, Y.; Wang, X.; Huang, J.; Yong, S. Research on Jiuzhaigou Ms 7.0 Earthquake based on AETA electromagnetic disturbance. *J. Peking Univ.* **2019**, *55*, 1007–1013. (In Chinese) [[CrossRef](#)]
31. Huang, J.; Wang, X.; Yong, S.; Feng, Y. A feature engineering framework for short-term earthquake prediction based on AETA data. In proceedings of the 2019 IEEE 8th Joint International Information Technology and Artificial Intelligence Conference (ITAIC), Chongqing, China, 24–26 May 2019; pp. 563–566. [[CrossRef](#)]
32. Bao, Z.; Yong, S.; Wang, X.; Yang, C.; Xie, J.; He, C. Seismic reflection analysis of AETA electromagnetic signals. *Appl. Sci.* **2021**, *11*, 5869. [[CrossRef](#)] [[CrossRef](#)]
33. Yi, G.; Long, F.; Liang, M.; Zhao, M.; Zhang, H.; Zhou, R.; Li, Y.; Liu, H.; Wu, P.; Wang, S.; et al. Seismogenic structure of the 5 September 2022 Sichuan Luding Ms6.8 earthquake sequence. *Chin. J. Geophys.* **2023**, *66*, 1363–1384. [[CrossRef](#)]
34. Qu, Z.; Zhu, B.; Cao, Y.; Fu, H. Rapid report of seismic damage to buildings in the 2022 M 6.8 Luding earthquake, China. *Earthq. Res. Adv.* **2023**, *3*, 20. [[CrossRef](#)] [[CrossRef](#)]
35. Peng, W.; Huang, X.; Wang, Z. Focal Mechanism and Regional Fault Activity Analysis of 2022 Luding Strong Earthquake Constraint by InSAR and Its Inversion. *Remote Sens.* **2023**, *15*, 3753. [[CrossRef](#)] [[CrossRef](#)]
36. Wen, X.Z.; Ma, S.L.; Xu, X.W.; He, Y.N. Historical pattern and behavior of earthquake ruptures along the eastern boundary of the Sichuan-Yunnan faulted-block, southwestern China. *Phys. Earth Planet. Inter.* **2008**, *168*, 16–36. [[CrossRef](#)] [[CrossRef](#)]
37. An, Y.; Wang, D.; Ma, Q.; Xu, Y.; Li, Y.; Zhang, Y.; Liu, Z.; Huang, C.; Su, J.; Li, J.; et al. Preliminary report of the 5 September 2022 MS 6.8 Luding earthquake, Sichuan, China. *Earthq. Res. Adv.* **2023**, *3*, 100184. [[CrossRef](#)] [[CrossRef](#)]
38. Wang, C.; Li, C.; Yong, S.; Wang, X.; Yang, C. Time Series and Non-Time Series Models of Earthquake Prediction Based on AETA Data: 16-Week Real Case Study. *Appl. Sci.* **2022**, *12*, 8536. [[CrossRef](#)] [[CrossRef](#)]
39. Bao, Z.; Zhao, J.; Huang, P.; Yong, S.; Wang, X. A deep learning-based electromagnetic signal for earthquake magnitude prediction. *Sensors* **2021**, *21*, 4434. [[CrossRef](#)] [[CrossRef](#)] [[PubMed](#)]

40. Wang, J.; Yong, S.; Wang, X. An AETA Electromagnetic Disturbance Anomaly Extraction Method based on Sample Entropy. In proceedings of the 2021 IEEE 5th Advanced Information Technology, Electronic and Automation Control Conference (IAEAC), Chongqing, China, 12–14 March 2021. [[CrossRef](#)]
41. Cao, J.; Zeng, L.; Zhan, F.; Wang, Z.; Wang, Y.; Chen, Y.; Meng, Q.; Ji, Z.; Wang, P.; Liu, Z.; et al. The electromagnetic wave experiment for CSES mission: Search coil magnetometer. *Sci. China Technol. Sci.* **2018**, *61*, 653–658. [[CrossRef](#)] [[CrossRef](#)]
42. Oropeza, V.; Sacchi, M. Simultaneous seismic data denoising and reconstruction via multichannel singular spectrum analysis. *Geophysics* **2011**, *76*, V25–V32. [[CrossRef](#)] [[CrossRef](#)]
43. Huang, W.; Wang, R.; Chen, Y.; Li, H.; Gan, S. Damped multichannel singular spectrum analysis for 3D random noise attenuation. *Geophysics* **2016**, *81*, V261–V270. [[CrossRef](#)] [[CrossRef](#)]
44. Voss, N.K.; Malservisi, R.; Dixon, T.H.; Protti, M. Slow slip events in the early part of the earthquake cycle. *J. Geophys. Res. Solid Earth* **2017**, *122*, 6773–6786. [[CrossRef](#)] [[CrossRef](#)]
45. Wallace, L.M.; Bartlow, N.; Hamling, I.; Fry, B. Quake clamps down on slow slip. *Geophys. Res. Lett.* **2014**, *41*, 8840–8846. [[CrossRef](#)] [[CrossRef](#)]
46. Rekapalli, R.; Tiwari, R.K. Windowed SSA (singular spectral analysis) for geophysical time series analysis. *J. Geol. Resour. Eng.* **2014**, *3*, 167–173. [[CrossRef](#)]
47. Gruszczynska, M.; Klos, A.; Rosat, S.; Bogusz, J. Deriving common seasonal signals in GPS position time series: By using multichannel singular spectrum analysis. *Acta Geodyn. Geomater.* **2017**, *14*, 267–278. [[CrossRef](#)] [[CrossRef](#)]
48. Oldham, S.; Fulcher, B.; Parkes, L.; Arnatkeviciute, A.; Suo, C.; Fornito, A. Consistency and differences between centrality measures across distinct classes of networks. *PloS ONE* **2019**, *14*, e0220061. [[CrossRef](#)] [[CrossRef](#)] [[PubMed](#)]
49. Zhang, Y.; Zhang, H.; Yang, Y.; Liu, N.; Gao, J. Seismic random noise separation and attenuation based on MVMD and MSSA. *IEEE Trans. Geosci. Remote Sens.* **2021**, *60*, 1–16. [[CrossRef](#)] [[CrossRef](#)]
50. Yu, Z.; Hattori, K.; Zhu, K.; Fan, M.; Marchetti, D.; He, X.; Chi, C. Evaluation of pre-earthquake anomalies of borehole strain network by using Receiver Operating Characteristic Curve. *Remote Sens.* **2021**, *13*, 515. [[CrossRef](#)] [[CrossRef](#)]
51. Kasahara, Y.; Muto, F.; Horie, T.; Yoshida, M.; Hayakawa, M.; Ohta, K.; Rozhnoi, A.; Solovieva, M.; Molchanov, O. On the statistical correlation between the ionospheric perturbations as detected by subionospheric VLF/LF propagation anomalies and earthquakes. *Nat. Hazards Earth Syst. Sci.* **2008**, *8*, 653–656. [[CrossRef](#)] [[CrossRef](#)]
52. Taylor, J.; Lester, M.; Yeoman, T. A superposed epoch analysis of geomagnetic storms. *Ann. Geophys.* **1994**, *12*, 612–624. [[CrossRef](#)] [[CrossRef](#)]
53. Hutchinson, J.A.; Wright, D.; Milan, S. Geomagnetic storms over the last solar cycle: A superposed epoch analysis. *J. Geophys. Res. Space Phys.* **2011**, *116*. [[CrossRef](#)] [[CrossRef](#)]
54. Maekawa, S.; Horie, T.; Yamauchi, T.; Sawaya, T.; Ishikawa, M.; Hayakawa, M.; Sasaki, H. A statistical study on the effect of earthquakes on the ionosphere, based on the subionospheric LF propagation data in Japan. *Ann. Geophys.* **2006**, *24*, 2219–2225. [[CrossRef](#)] [[CrossRef](#)]
55. Han, P.; Hattori, K.; Hirokawa, M.; Zhuang, J.; Chen, C.H.; Febriani, F.; Yamaguchi, H.; Yoshino, C.; Liu, J.Y.; Yoshida, S. Statistical analysis of ULF seismomagnetic phenomena at Kakioka, Japan, during 2001–2010. *J. Geophys. Res. Space Phys.* **2014**, *119*, 4998–5011. [[CrossRef](#)] [[CrossRef](#)]
56. Wu, L.; Wang, X.; Qi, Y.; Lu, J.; Mao, W. Characteristics and mechanisms of near-surface atmospheric electric field negative anomalies preceding the 5 September, 2022, Ms6.8 Luding earthquake, China. *EGU Sphere* **2023**, *2023*, 1–17. [[CrossRef](#)]
57. Zhu, J.; Sun, K.; Zhang, J. Anomalies in Infrared Outgoing Longwave Radiation Data before the Yangbi Ms 6.4 and Luding Ms 6.8 Earthquakes Based on Time Series Forecasting Models. *Appl. Sci.* **2023**, *13*, 8572. [[CrossRef](#)] [[CrossRef](#)]
58. Liu, J.; Zhang, X.; Yang, X.; Yang, M.; Zhang, T.; Bao, Z.; Wu, W.; Qiu, G.; Yang, X.; Lu, Q. The Analysis of Lithosphere–Atmosphere–Ionosphere Coupling Associated with the 2022 Luding Ms6.8 Earthquake. *Remote Sens.* **2023**, *15*, 4042. [[CrossRef](#)] [[CrossRef](#)]

Disclaimer/Publisher’s Note: The statements, opinions and data contained in all publications are solely those of the individual author(s) and contributor(s) and not of MDPI and/or the editor(s). MDPI and/or the editor(s) disclaim responsibility for any injury to people or property resulting from any ideas, methods, instructions or products referred to in the content.